SUPPORTING INFORMATION

Crystal Engineering and Ferroelectricity at the Nanoscale in Epitaxial 1D Manganese Oxide on Silicon

Andrés Gomez[1γ], José Manuel Vila-Fungueiriño[2,3γ], Claire Jolly[2], Ricardo Garcia-Bermejo[2], Judith Oró-Solé[1], Etienne Ferain[4], Narcís Mestres[1], César Magén[5], Jaume Gazquez[1], Juan Rodriguez-Carvajal[6], and Adrián Carretero-Genevrier[2]*.

1. Andres Gomez, Dr. Judith Oró-Solé, Dr. Jaume Gazquez, Dr. Narcis Mestres.
Institut de Ciència de Materials de Barcelona ICMAB, Consejo Superior de Investigaciones Científicas CSIC, Campus UAB 08193 Bellaterra, Catalonia, Spain
2. Dr. Adrian Carretero-Genevrier, Claire Jolly, Dr. Ricardo Bermejo, Dr. José Manuel Vila-Fungueiriño.
Institut d'Electronique et des Systemes (IES), CNRS, Université de Montpellier, 860 Rue de Saint Priest 34095 Montpellier, France
3. Dr. José Manuel Vila-Fungueiriño
Centro Singular de Investigación en Química Biolóxica e Materiais Moleculares (CiQUS). C/ Jenaro de la Fuente s/n Campus Vida. Universidade de Santiago de Compostela. 15782, Santiago de Compostela, Galicia, Spain
4. Dr. Etienne Ferain,
it4ip S.A., avenue J.-E. Lenoir, 1, 1348 Louvain-la-Neuve, Belgium.
5. Dr. César Magén.
Instituto de Ciencia de Materiales de Aragón (ICMA), Universidad de Zaragoza – CSIC, Departamento de Física de la Materia Condensada, Universidad de Zaragoza, 50009 Zaragoza, Spain.
Laboratorio de Microcopías Avanzadas (LMA), Instituto de Nanociencia de Aragón (INA), Universidad de Zaragoza, 50018 Zaragoza, Spain.
6. Dr. Juan Rodriguez-Carvajal.
Institut Laue-Langevin, 71 Avenue des Martyrs, CS 20156, 38042, Grenoble, Cedex 9, France

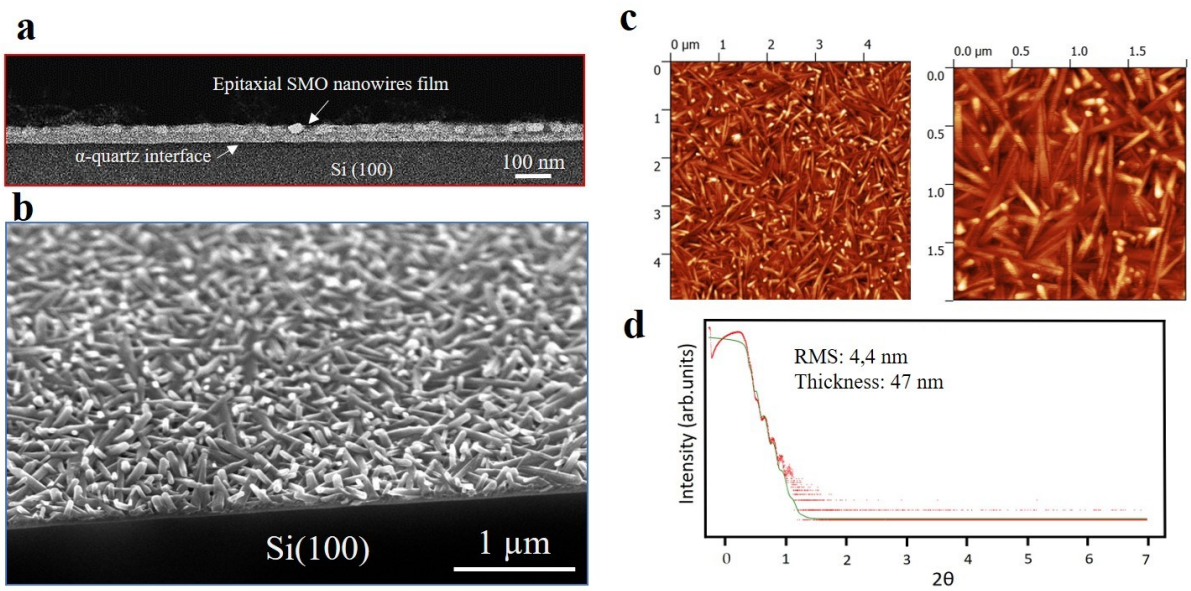

Figure S1. (a) Cross-sectional low-resolution HAADF-STEM image of the nanowire film (b) Cross-sectional tilted SEM-FEG image of an epitaxial $Sr_{1+\delta}Mn_8O_{16}$ nanowire film on a silicon substrate (c) AFM topographic characterization of a SMO nanowire thin film. (d) X-ray reflectometry analysis of a SMO nanowire film showing a RMS of 4.4 nm and a thickness of 47 nm.

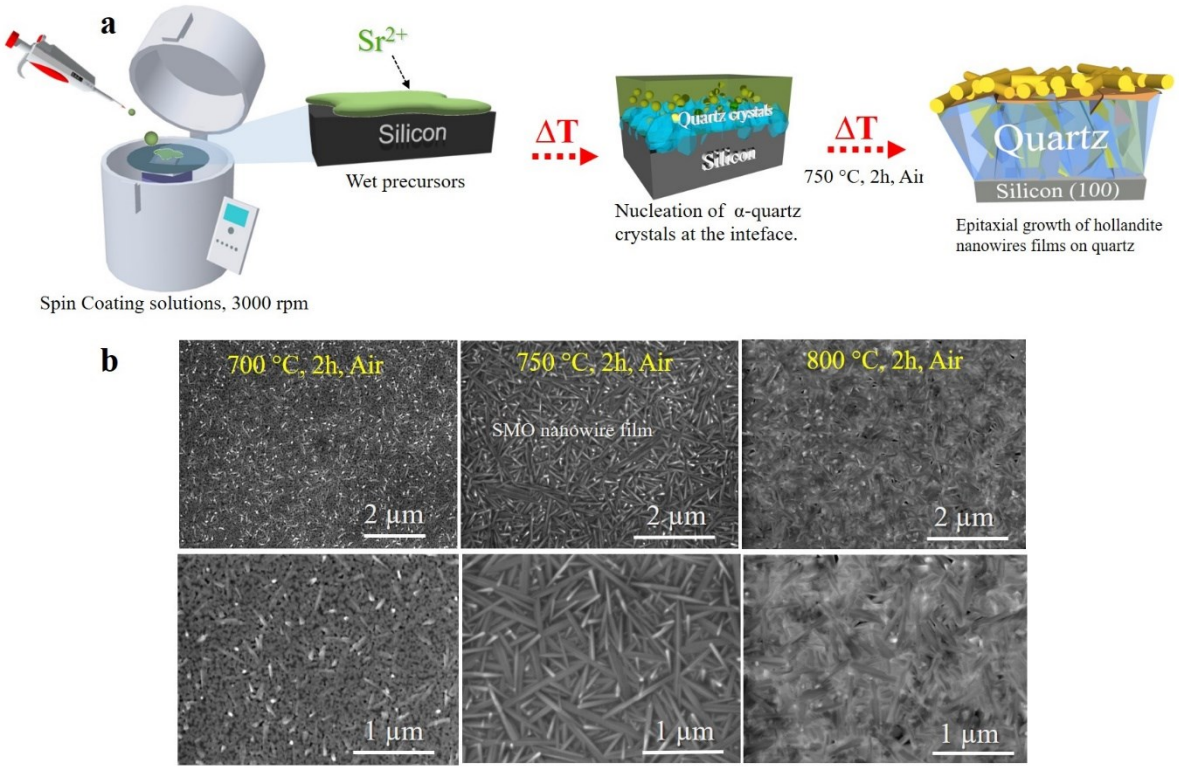

Figure S2. Growth mechanism and synthesis methods of SMO nanowire thin film on silicon Si (100) substrates. (a) Schematics representation of the different steps growth of epitaxial SMO nanowires i.e. (i) a first stage where a film chemical precursor solution containing Sr^{2+} melting agents and Mn^{4+} salt is deposited on a Si substrate by using spin-coating technique; (ii) next step involves the 2D-confined nucleation in thin film form of oxide nanowires seeds and first devitrification and nucleation of disoriented quartz crystals at the silicon interface; (iii) finally α-quartz film formation at higher temperatures (750 °C), allowing the epitaxial stabilization of SMO hollandite-like nanowire thin film. (b) Series of FEG-SEM images showing the crystallization and growth of SMO nanowire film on silicon at different temperatures.

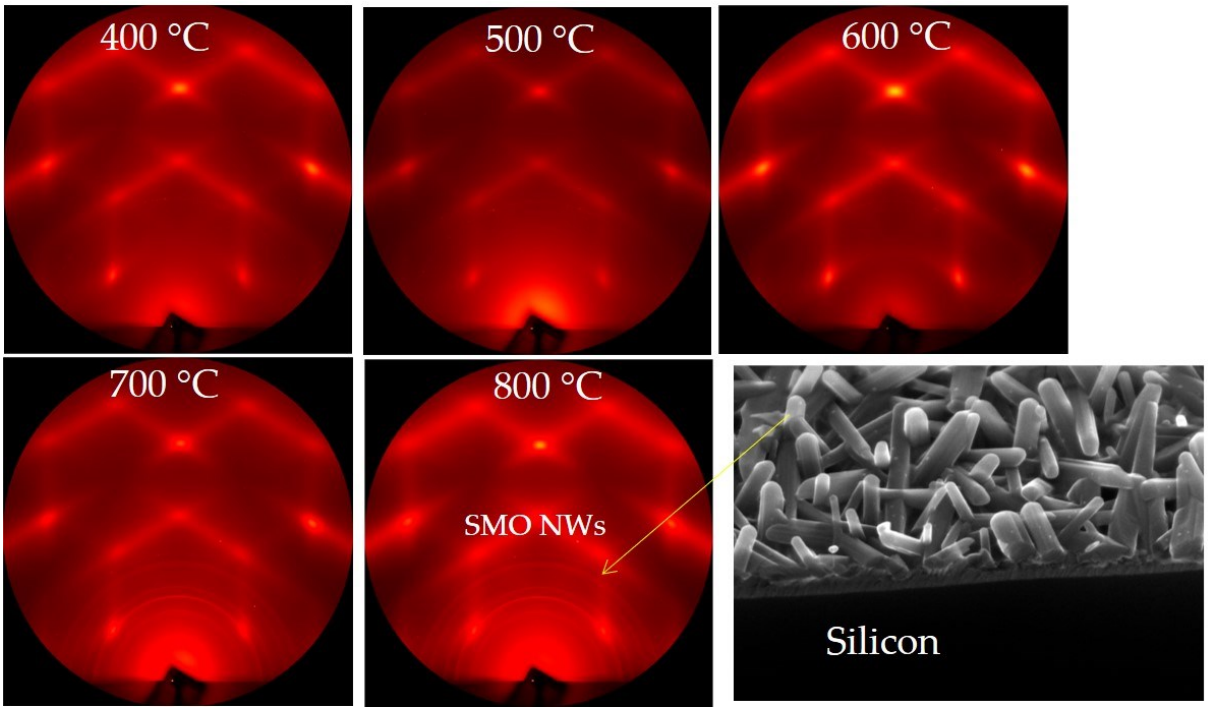

Figure S3. Observation of the SMO nanowires crystallization thin films on silicon by temperature-resolved synchrotron X-ray diffraction. The diffraction pattern is dominated by the thermal diffuse scattering of silicon, the Debye-Scherrer rings observed clearly at 700°C and 800°C correspond to the diffraction pattern of SMO nanowires.

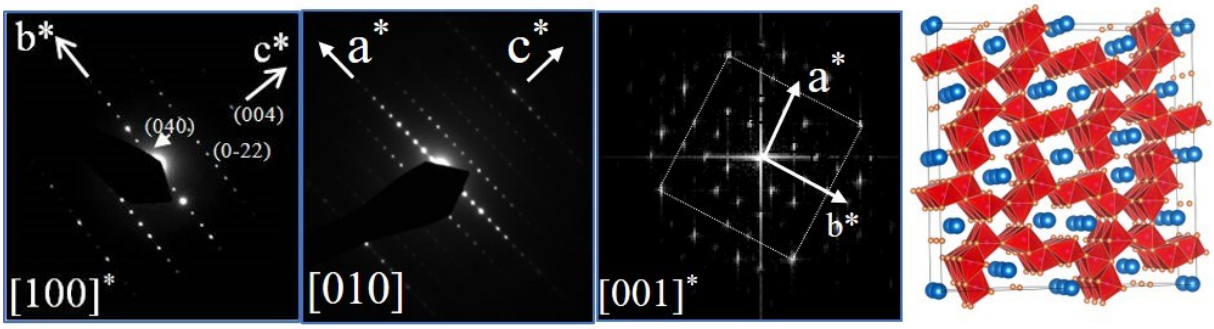

Figure. S4. The three basis planes of the SMO crystallographic unit cell. Notice that the diffraction patterns for the Sr-case do not present satellites or prominent diffuse scattering. The doubling of the c-axis with respect to the $Ba_{6-x}Mn_{24}O_{48}$ is well established in the electron diffraction patterns of our compound. In the structure show which color corresponds to each cation.

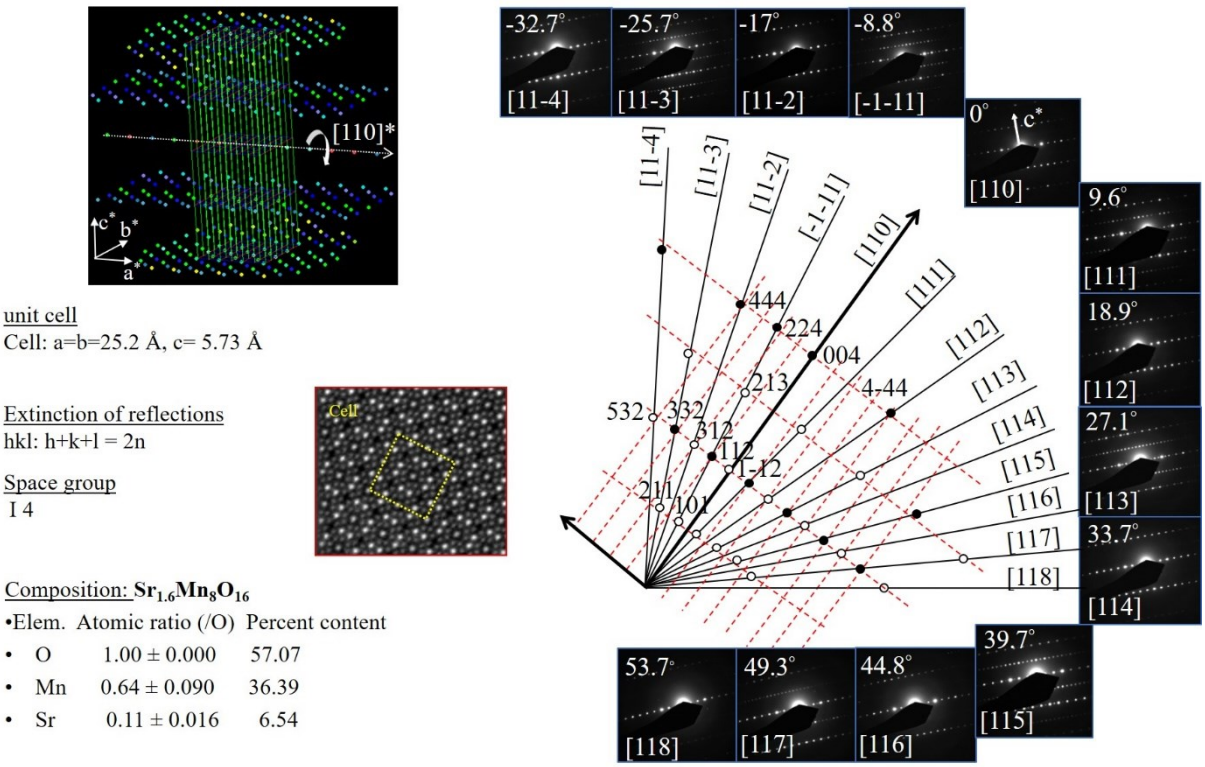

Figure S5. Reciprocal space reconstruction along the [110] crystallographic direction of a single SMO nanowire by using electron diffraction. Electron diffraction spots in the reciprocal space show that (hkl) reflection conditions and systematic absences can be indexed in a pseudo-tetragonal body centered cell with lattice parameters $a = 25.2$ Å, $c = 5.7$ Å, $\alpha = \beta = \gamma = 90$ º compatible with a non-centrosymmetric space group *I4*. EDX analysis of the SMO structure showed a composition $Sr_{1.4}Mn_8O_{16}$.

Table S1

Atomic positions of the model explaining the atomic-resolution STEM images that correspond to the non-centrosymmetric polar space group *I*4 with unit cell parameters a_T=25.488 Å, c_T=5.753 Å. The letter "h" in the label of atoms indicates that the atom belongs to the hollandite blocks or within the hollandite tunnels. The letter "p" indicates that the atom belongs to the pyrolusite blocks. The letter "m" indicates that the atom is shared by the pyrolusite and hollandite blocks and the letter "c" indicates that the atoms are inside the new tunnels. Coordinates of different atom in the input structure are frequently equal in value because we have constructed the model from the centrosymmetric structure described in [1]. Only the Sr-atoms break the centre of symmetry of the global structure in the input structure. The optimized crystal structure against bond-valence in the space group *I*4 breaks the inversion centre with all atoms and it does not change too much the positions. The standard deviations in the positions of the relaxed structure correspond to the fluctuations intrinsic to the optimization algorithm. The calculated bond-valence sums and global instability indices are provided after the table of atom positions.

Note: Using the composition, $Sr_3Mn_{12}O_{24}$ (or $Sr_2Mn_8O_{16}$) we have optimized the position of the atoms using the program *GLOpSAnn*, distributed within the *FullProf Suite* [2], which allows applying different kind of cost functions to structural solution, or optimisation using Simulated Annealing followed by local optimization. As we do not have adequate diffraction data, we have used bond-valence and anti-bump as cost functions to be optimized against atom positions. In order to prevent too short atom contacts, the anti-bump penalty function $ab=(d_{min}/d)^{12}$ has been used for each pair of chemical element

(see documentation of *GLOpSAnn*). We have started with the ideal generated atom positions by the program *Similar* (coordinate triplets on the left of the table) and we have allowed the atoms to move within a box of 0.2 Å side in the three spatial directions around the input positions. With that method, we get a final crystal structure, close to the input structure, that minimizes the difference between the ionization state number and the bond-valence sums around each ion. We have assumed bond-valence parameters for Mn^{4+}, Mn^{3+}, Sr^{+2} and O^{2-}, placing the Mn^{4+} in the pyrolusite blocks. In the real compound, the composition has to be adapted by diminishing the occupation factors of the Sr within the hollandite tunnels.

Atom	Type	x/a	y/b	z/c	Wyckoff site	x/a	y/b	z/c
Srh1	Sr	0.50000	0.50000	0.00000	(2a)	0.50000	0.50000	-0.0058(3)
Srh2	Sr	0.50000	0.00000	0.23300	(4b)	0.50000	0.00000	0.2265(3)
Src3	Sr	0.57316	0.74297	0.50000	(8c)	0.56921(5)	0.74666(5)	0.4935(2)
Src4	Sr	0.42623	0.75970	0.49708	(8c)	0.56999(7)	0.23882(4)	-0.0081(2)
Mnp1	Mn	0.18750	0.18062	0.25000	(8c)	0.18428(5)	0.17720(7)	0.2660(2)
Mnp2	Mn	0.18750	0.18062	0.75000	(8c)	0.19179(4)	0.17795(6)	0.7619(3)
Mnp3	Mn	0.68749	0.18061	0.00000	(8c)	0.68886(6)	0.17874(5)	0.0158(3)
Mnp4	Mn	0.68749	0.18061	0.50000	(8c)	0.68831(7)	0.17683(5)	0.5174(2)
Mnh1	Mn	0.11010	0.10522	0.00000	(8c)	0.11090(4)	0.10152(7)	-0.0034(3)
Mnh2	Mn	0.11010	0.10522	0.50000	(8c)	0.11218(7)	0.10209(5)	0.5032(2)
Mnh3	Mn	0.61011	0.10522	0.25000	(8c)	0.61121(6)	0.10144(6)	0.2466(2)
Mnh4	Mn	0.61011	0.10522	0.75000	(8c)	0.60601(7)	0.10380(7)	0.7345(3)
Mnh5	Mn	0.51300	0.86000	0.00000	(8c)	0.51281(4)	0.85583(4)	0.0145(3)
Mnh6	Mn	0.51300	0.86000	0.50000	(8c)	0.50945(4)	0.85615(6)	0.5127(2)
Mnh7	Mn	0.51300	0.36000	0.25000	(8c)	0.51172(3)	0.35645(7)	0.2417(3)
Mnh8	Mn	0.51300	0.36000	0.75000	(8c)	0.51053(6)	0.35588(5)	0.7550(3)
Op1	O	0.76310	0.82521	0.00000	(8c)	0.76722(5)	0.82221(7)	-0.0170(2)
Op2	O	0.76310	0.82521	0.50000	(8c)	0.76687(5)	0.82128(5)	0.5095(3)
Op3	O	0.26310	0.82521	0.25000	(8c)	0.26646(6)	0.82275(7)	0.2344(3)
Op4	O	0.26310	0.82521	0.75000	(8c)	0.26675(5)	0.82358(6)	0.7353(2)
Om1	O	0.63633	0.67670	0.00000	(8c)	0.64046(6)	0.68100(3)	-0.0163(3)
Om2	O	0.63633	0.67670	0.50000	(8c)	0.63998(8)	0.68092(4)	0.5056(3)
Om3	O	0.63633	0.17670	0.25000	(8c)	0.64050(6)	0.18057(6)	0.2325(3)
Om4	O	0.63633	0.17670	0.75000	(8c)	0.63996(7)	0.18068(4)	0.7327(2)
Om5	O	0.59750	0.84062	0.00000	(8c)	0.60110(8)	0.83713(4)	0.0156(3)
Om6	O	0.59750	0.84062	0.50000	(8c)	0.60149(6)	0.83650(4)	0.4957(3)
Om7	O	0.59751	0.34061	0.25000	(8c)	0.60121(6)	0.33651(6)	0.2561(3)
Om8	O	0.59751	0.34061	0.75000	(8c)	0.60094(6)	0.33677(5)	0.7505(2)
Oh1	O	0.62108	0.94023	0.00000	(8c)	0.62140(8)	0.94180(7)	-0.0116(3)
Oh2	O	0.62108	0.94023	0.50000	(8c)	0.62099(7)	0.93909(7)	0.5004(3)
Oh3	O	0.12108	0.94023	0.25000	(8c)	0.12133(8)	0.94091(6)	0.2489(3)
Oh4	O	0.12108	0.94023	0.75000	(8c)	0.11760(7)	0.93949(6)	0.7395(3)
Oh5	O	0.09046	0.02477	0.00000	(8c)	0.08826(7)	0.02554(6)	0.0029(3)
Oh6	O	0.09046	0.02477	0.50000	(8c)	0.08674(7)	0.02300(4)	0.5009(3)
Oh7	O	0.59045	0.02477	0.25000	(8c)	0.58693(8)	0.02794(6)	0.2556(4)
Oh8	O	0.59045	0.02477	0.75000	(8c)	0.58910(3)	0.02522(6)	0.7635(3)
Oh9	O	0.50488	0.68855	0.00000	(8c)	0.50205(6)	0.69283(6)	0.0105(3)
Oh10	O	0.50488	0.68855	0.50000	(8c)	0.50285(5)	0.69245(5)	0.4987(3)
Oh11	O	0.50488	0.18855	0.25000	(8c)	0.50679(7)	0.19255(6)	0.2349(3)
Oh12	O	0.50488	0.18855	0.75000	(8c)	0.50717(6)	0.19201(7)	0.7596(3)

Calculated average distances distortion and bond-valence sums, for all the atoms in the asymmetric unit, of the initial idealized model generated by the program *Similar* from the *I*4/*m* model of $Ba_{6-x}Mn_{24}O_{48}$ [1], after transforming the unit cell $\mathbf{a}_B$ =18.173(2) Å, $\mathbf{c}_B$ =2.836(1) to $\mathbf{a}_T = \mathbf{a}_B + \mathbf{b}_B$, $\mathbf{b}_T = -\mathbf{a}_B + \mathbf{b}_B$ and $\mathbf{c}_T = 2\mathbf{c}_B$. We have adjusted the cell parameters to a_T=25.488 Å, c_T=5.753 Å in the space group *I*4. The global instability index is 12.14%.

Atom	Coord	D_aver	Sigm	Distort(x10-4)	Valence	BVSum(Sigma)
Srh1	4.00	2.3906(	0)	0.001	2.000	1.915(0)
Srh2	4.00	2.3923(	0)	0.000	2.000	1.906(0)
Src3	7.00	2.7375(	0)	143.151	2.000	1.964(0)
Src4	9.00	2.7862(	0)	35.039	2.000	1.612(0)
Mnp1	6.00	2.0144(	0)	37.237	4.000	3.111(0)
Mnp2	6.00	2.0144(	0)	37.237	4.000	3.111(0)
Mnp3	6.00	2.0144(	0)	37.254	4.000	3.110(0)
Mnp4	6.00	2.0144(	0)	37.254	4.000	3.110(0)
Mnh1	6.00	1.9716(	0)	11.022	3.000	3.436(0)
Mnh2	6.00	1.9716(	0)	11.022	3.000	3.436(0)
Mnh3	6.00	1.9715(	0)	11.067	3.000	3.437(0)
Mnh4	6.00	1.9715(	0)	11.067	3.000	3.437(0)
Mnh5	6.00	1.9840(	0)	26.248	3.000	3.382(0)
Mnh6	6.00	1.9840(	0)	26.248	3.000	3.382(0)
Mnh7	6.00	1.9839(	0)	26.319	3.000	3.383(0)
Mnh8	6.00	1.9839(	0)	26.319	3.000	3.383(0)
Op1	3.00	1.9873(	0)	24.821	-2.000	1.646(0)
Op2	4.00	2.1507(	0)	188.972	-2.000	1.890(0)
Op3	4.00	2.2423(	0)	402.312	-2.000	1.737(0)
Op4	4.00	2.2423(	0)	402.312	-2.000	1.737(0)
Om1	3.00	1.9430(	0)	0.007	-2.000	1.807(0)
Om2	4.00	2.0406(	0)	68.702	-2.000	2.365(0)
Om3	4.00	2.1424(	0)	260.373	-2.000	1.993(0)
Om4	4.00	2.1424(	0)	260.373	-2.000	1.993(0)
Om5	4.00	2.0712(	0)	53.889	-2.000	1.867(0)
Om6	5.00	2.1700(	0)	122.159	-2.000	2.166(0)
Om7	5.00	2.2453(	0)	276.425	-2.000	1.974(0)
Om8	5.00	2.2453(	0)	276.425	-2.000	1.974(0)
Oh1	3.00	1.9517(	0)	1.631	-2.000	1.791(0)
Oh2	4.00	2.2452(	0)	513.407	-2.000	1.857(0)
Oh3	3.00	1.9516(	0)	1.622	-2.000	1.791(0)
Oh4	3.00	1.9516(	0)	1.622	-2.000	1.791(0)
Oh5	3.00	1.9951(	0)	16.809	-2.000	1.626(0)
Oh6	4.00	2.0940(	0)	78.326	-2.000	2.105(0)
Oh7	4.00	2.0945(	0)	78.824	-2.000	2.102(0)
Oh8	4.00	2.0945(	0)	78.824	-2.000	2.102(0)
Oh9	3.00	2.1830(	0)	225.290	-2.000	1.432(0)
Oh10	3.00	2.0427(	0)	40.041	-2.000	1.940(0)
Oh11	4.00	2.3911(	0)	366.968	-2.000	1.519(0)
Oh12	4.00	2.3911(	0)	366.968	-2.000	1.519(0)

Normalized GII(b)=SUM {|BVS-abs(q)|*mult/abs(q)}/N_Atoms_UCell = 12.14 %

Calculated average distances, distortion and bond-valence sums, for all the atoms in the asymmetric unit, of the optimized model obtained by the program *GLOpSAnn*, in the space group *I*4. The global instability index is 4.53%.

Atom	Coord	D_aver Sigm	Distort(x10-4)	Valence	BVSum(Sigma)
Srh1	4.00	2.2876(7)	-0.001	2.000	2.529(5)
Srh2	4.00	2.3516(9)	0.602	2.000	2.130(5)
Src3	7.00	2.7397(7)	162.876	2.000	2.018(5)
Src4	9.00	2.7451(7)	69.191	2.000	2.000(5)
Mnp1	6.00	1.9643(9)	91.033	4.000	3.825(10)
Mnp2	6.00	1.9706(9)	116.282	4.000	3.914(10)
Mnp3	6.00	1.9685(8)	96.332	4.000	3.832(11)
Mnp4	6.00	1.9753(8)	111.408	4.000	3.819(10)
Mnh1	6.00	2.0182(9)	12.007	3.000	3.037(7)
Mnh2	6.00	2.0251(8)	16.634	3.000	3.003(7)
Mnh3	6.00	2.0170(9)	10.275	3.000	3.039(8)
Mnh4	6.00	2.0171(10)	18.543	3.000	3.077(9)
Mnh5	6.00	2.0391(9)	49.791	3.000	3.027(8)
Mnh6	6.00	2.0538(9)	75.618	3.000	3.004(8)
Mnh7	6.00	2.0402(9)	54.138	3.000	3.022(8)
Mnh8	6.00	2.0421(9)	58.461	3.000	3.021(8)
Op1	3.00	2.0061(11)	194.350	-2.000	2.002(7)
Op2	4.00	2.1985(10)	369.860	-2.000	2.001(7)
Op3	4.00	2.2763(11)	546.788	-2.000	1.984(8)
Op4	4.00	2.2810(9)	574.045	-2.000	2.001(7)
Om1	3.00	1.9630(11)	105.445	-2.000	2.000(7)
Om2	4.00	2.1062(11)	120.393	-2.000	2.073(7)
Om3	4.00	2.1654(11)	256.989	-2.000	2.000(7)
Om4	4.00	2.1751(11)	282.973	-2.000	1.988(7)
Om5	4.00	2.0725(11)	45.253	-2.000	1.823(6)
Om6	5.00	2.1948(9)	72.881	-2.000	1.996(5)
Om7	5.00	2.2660(9)	320.709	-2.000	1.929(6)
Om8	5.00	2.2534(9)	290.426	-2.000	1.941(5)
Oh1	3.00	1.9161(14)	15.191	-2.000	2.008(8)
Oh2	4.00	2.2304(12)	410.095	-2.000	1.792(6)
Oh3	3.00	1.9820(13)	16.977	-2.000	1.689(6)
Oh4	3.00	1.9638(13)	2.055	-2.000	1.735(6)
Oh5	3.00	2.0597(13)	1.948	-2.000	1.338(5)
Oh6	4.00	2.1223(10)	22.684	-2.000	1.947(5)
Oh7	4.00	2.1240(12)	38.522	-2.000	1.932(6)
Oh8	4.00	2.1241(9)	44.782	-2.000	1.906(5)
Oh9	3.00	2.1156(13)	197.880	-2.000	1.680(6)
Oh10	3.00	2.0349(12)	27.057	-2.000	2.000(6)
Oh11	4.00	2.3083(11)	299.376	-2.000	1.793(6)
Oh12	4.00	2.3075(11)	306.586	-2.000	1.777(6)

Normalized GII(b)= SUM {|BVS-abs(q)|*mult/abs(q)}/N_Atoms_UCell = 4.53 %

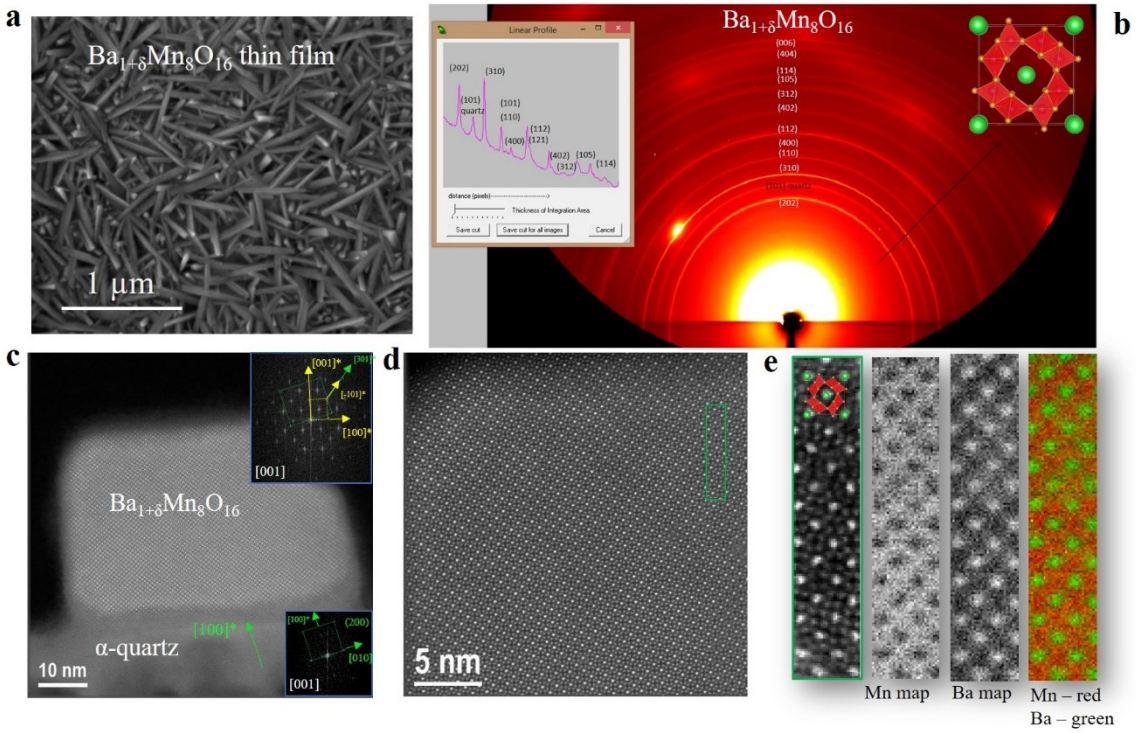

Figure S6. Chemical growth of epitaxial Barium oxide hollandite nanowire film on silicon. (a) FEG-SEM image showing the microstructural aspect and homogeneity of the $Ba_{1+\delta}Mn_8O_{16}$ thin films. (b) Grazing incidence 2D synchrotron X-ray diffractometer of a $Ba_{1+\delta}Mn_8O_{16}$ nanowire film. Notice that with this technique we are able to observe all the reflections corresponding to the monoclinic crystallographic structure without any secondary phases. (c) HAADF-STEM image of a $Ba_{1+\delta}Mn_8O_{16}$ nanowire along the longitudinal nanowire axis i.e. [010] crystallographic direction epitaxially grown on top of the α-quartz layer. The insets show the FFT images that indicates the epitaxial relationship between both phases i.e. (110) SMO [-101] // (110) α-quartz [301] (d) Detailed HAADF-STEM image of a $Ba_{1+\delta}Mn_8O_{16}$ nanowire along the longitudinal nanowire axis i.e. [010] crystallographic direction. (e) EELS atomic-resolution chemical mapping of Mn and Ba elements of a $BaMn_8O_{16}$ nanowire along the [010] crystallographic direction.

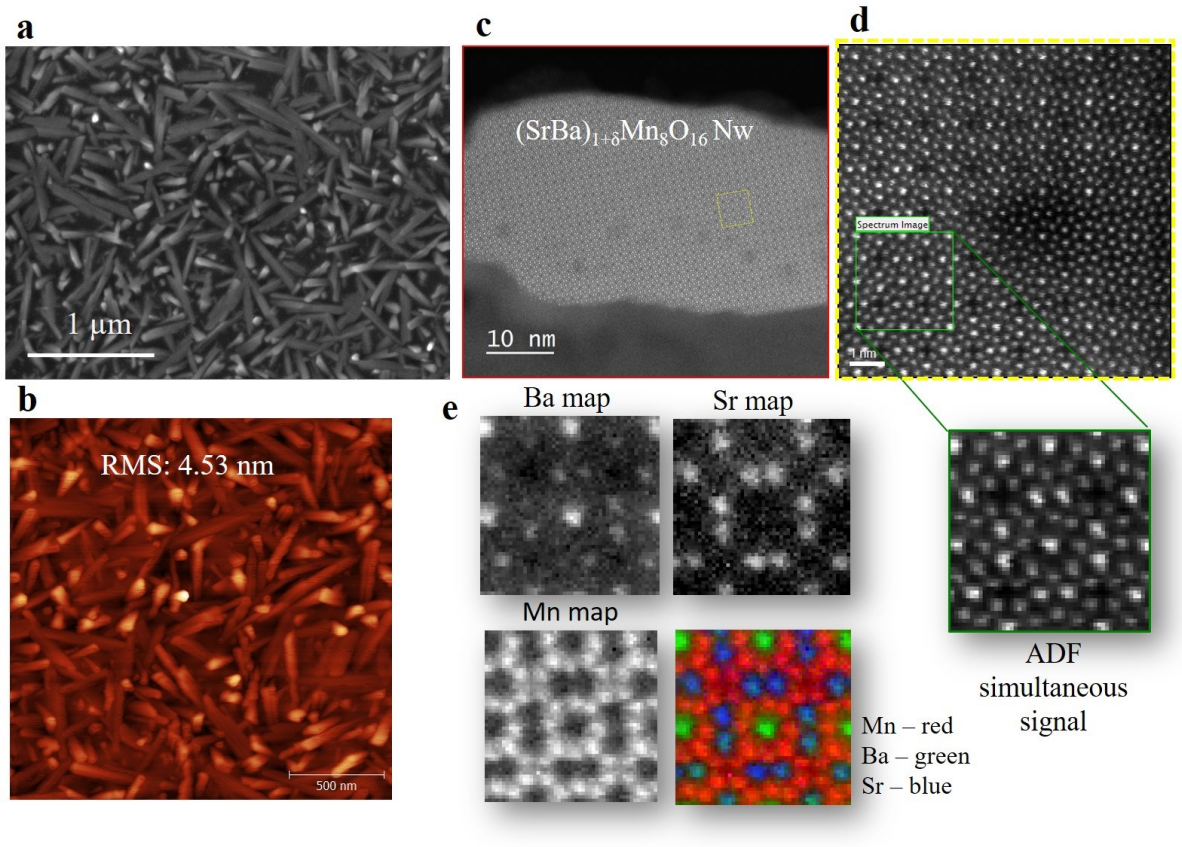

Figure S7. Chemical growth of Barium-doped SMO manganite nanowire film on silicon. Serie of FEG-SEM (a) and AFM (b) images showing the microstructural aspect, homogeneity and roughness of the thin film. (c) HAADF-STEM image of a BSMO nanowire along the longitudinal nanowire axis i.e. [001] crystallographic direction epitaxially grown on top of the α-quartz layer. (d). HAADF-STEM images of a BSMO nanowire along the longitudinal nanowire axis i.e. [001] crystallographic direction epitaxially grown on top of the α-quartz layer. (e) EELS atomic-resolution chemical mapping of Mn, Sr and Ba elements of a BSMO nanowire along the [001] crystallographic direction

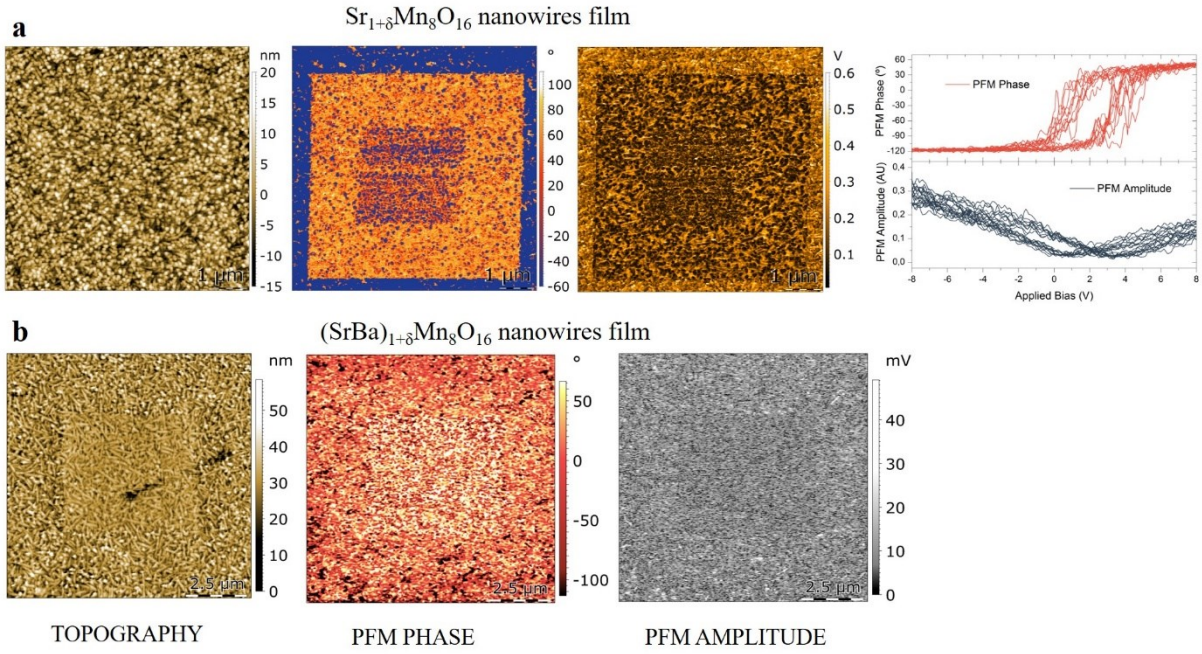

Figure S8. Comparative PFM study between the isostructural BSMO and the SMO hollandite nanowire film. (a) Topographic AFM image, VPFM Phase and VPFM amplitude signals respectively confirming the switching of the SMO nanowire film using a bias of ±20 VDV due to the ferroelectric nature of this nanowires. (b) Topographic AFM image, VPFM-Phase and VPFM-Amplitude signals of the Barium doped SMO nanowire film respectively that show no differences on the contrast due to a ferroelectricity free behavior.

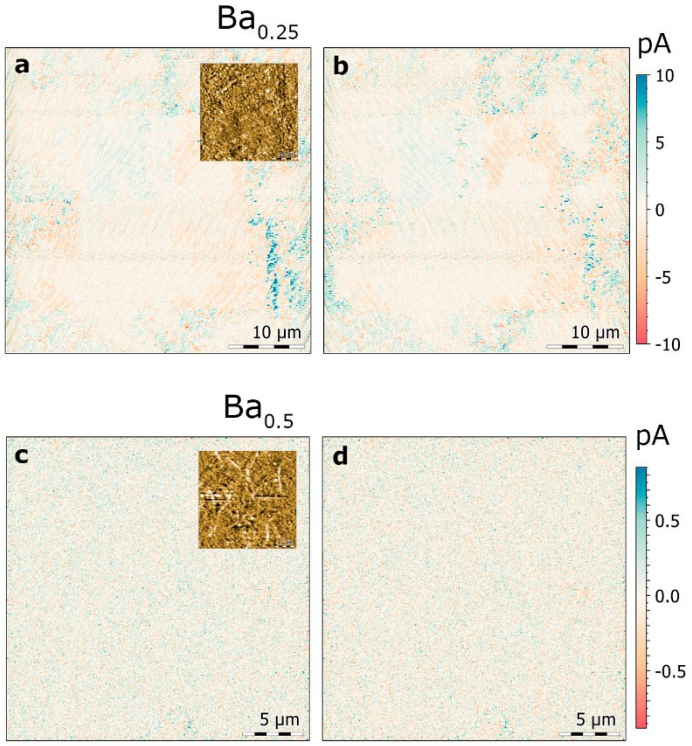

Figure S9. DPFM measurements Matrix of the Ba dope SMO samples. DPFM-Si (a) and DPMF-So (b) of a 0.25 Ba sample, with topography AFM image as insert. Both images show a similar contrast, meaning only leakage current is found in the sample and there is no ferroelectric response pattern. DPFM-Si (a) and DPMF-So (b) of a 0.5 Ba sample, for this case the leakage current is in the detection level of our amplifier, while there is still no ferroelectric response.

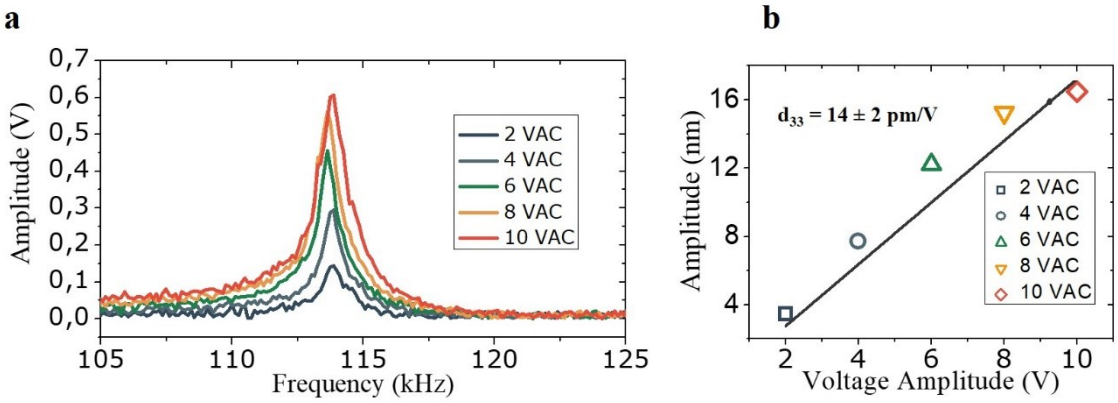

Figure S10. Measurement of d_{33} piezoelectric coefficient of SMO nanowire film by using PFM study. (a) PFM measure at different voltages of a SMO nanowire film. (b) The data shows a linear increase of the PFM resonant frequency amplitude with an increase of the applied AC bias, confirming the piezoelectric functionality of a SMO nanowire film. Importantly, this indirect measure gives a similar value to that of DPFM direct method.

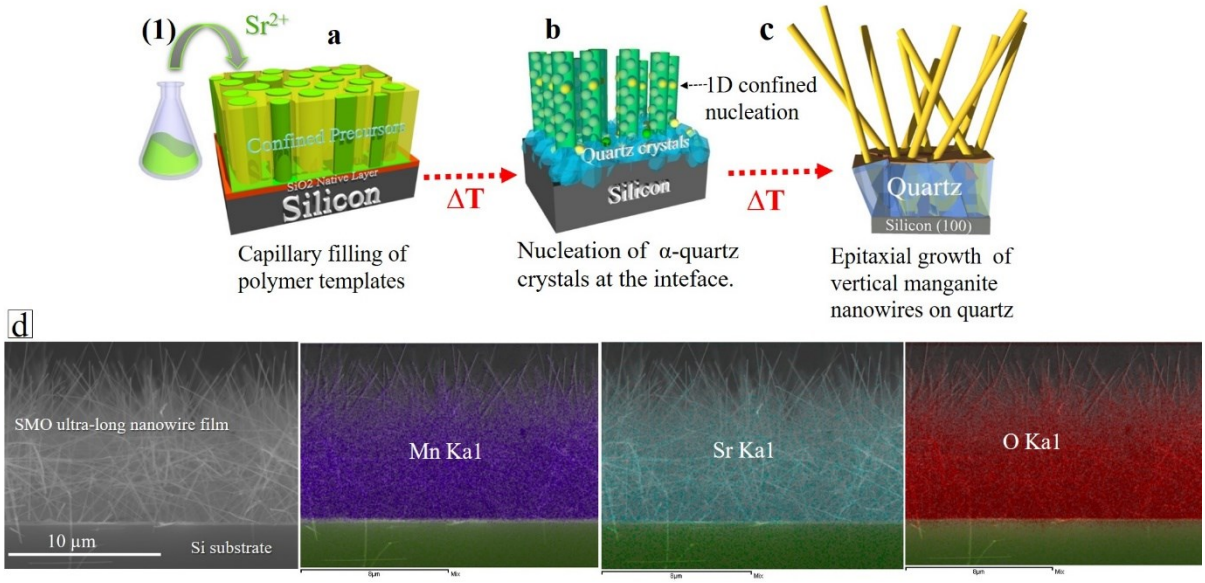

Figure S11. Growth mechanism and synthesis method of SMO ultra-long vertical nanowire thin film on silicon Si (100) substrate. Schematics representing the different steps growth of ultra-long vertical

epitaxial SMO nanowire i.e. (a) a first stage where a nanoporous polymer template is deposited on Si substrate filled with the chemical precursor solution containing Sr^{2+} melting agents and Mn salt. (b) 1D-confined nucleation in high aspect ratio nanopores of oxide nanowires seeds and first devitrification and nucleation of disoriented quartz crystals at the silicon interface. (c) α-quartz film formation at higher temperatures (800 °C), allowing the epitaxial stabilization of oxide nanowires[3]. (d) Cross-sectional FEG-SEM image of vertical ultralong SMO nanowire film grown on silicon substrate together with the chemical analysis of Mn, Sr and O element.

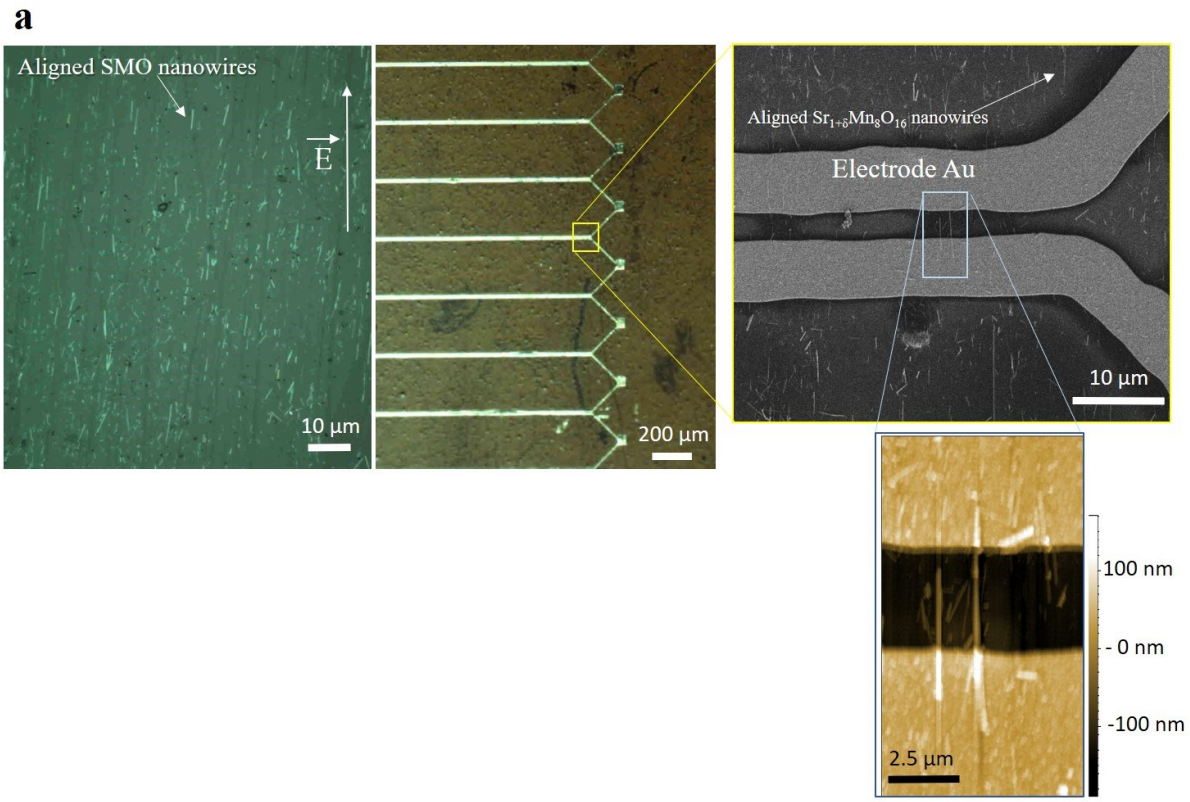

Figure S12. Transfer, alignment and contact of single SMO ultra-long nanowires on flexible Kapton substrate (optical, SEM and AFM topographic images respectively).

References

[1] Ph. Boullay, M Hervieu, and B. Raveau. *A New Manganite with an Original Composite Tunnel Structure: $Ba_6Mn_{24}O_{48}$*, *Journal of Solid State Chemistry* **132**, 239-248 (1997).

[2] Juan Rodriguez-Carvajal, FULLPROF: *A program for Rietveld refinement and pattern matching analyses*. Abstracts of the satellite meeting on powder diffraction of the XVth congress of the International Union of

Crystallography, Toulouse, France, 1990; International Union of Crystallography: Chester, England, 1990; p 127.

See also: Juan Rodríguez-Carvajal, *Recent Advances in Magnetic-Structure Determination by Neutron Powder Diffraction*. *Physica B* **192**, 55-69 (1993).

The *FullProf Suite* can be downloaded from https://www.ill.eu/sites/fullprof/php/downloads.html